Available online at www.sciencedirect.com
SCIENCE DIRECT®
ELSEVIER
Optics and Lasers in Engineering 43 (2005) 951–962
OPTICS and LASERS in ENGINEERING

# Investigation of dynamic displacements of lithographic press rubber roller by time average geometric moiré

Minvydas Ragulskis[a,*], Rimas Maskeliunas[b], Liutauras Ragulskis[c], Vytautas Turla[b]

[a]*Kaunas University of Technology, Department of Mathematical Research in Systems, Studentu 50-222, Kaunas LT-51368, Lithuania*
[b]*Vilnius Gediminas Technical University, Department of Printing Machines, J. Basanaviciaus 28, Vilnius LT-03224, Lithuania*
[c]*Vytautas Magnus University, Department of Informatics, Vileikos 8, Kaunas LT-44404, Lithuania*

Received 1 July 2004; received in revised form 1 October 2004; accepted 1 October 2004
Available online 24 December 2004

**Abstract**

Geometric moiré fringe formation method is a classical well-established experimental technique with numerous practical applications. This paper proposes the application of time-average geometric moiré analysis for the determination of dynamic displacements of the lithographic press rubber roller. This optical measurement technique is a natural extension of double-exposure geometric moiré for the identification of dynamic displacements of vibrating elastic structures. Experimental investigations prove the validity and effective practical applicability of the method.


*Keywords:* Geometric moiré; Fringes; Time average; Vibration; Press roller

*Corresponding author. Tel.: +370 698 22456; fax: +370 373 30446.
*E-mail address:* minvydas.ragulskis@ktu.lt (M. Ragulskis).

0143-8166/$ - see front matter © 2004 Elsevier Ltd. All rights reserved.
doi:10.1016/j.optlaseng.2004.10.004

## 1. Introduction

Double-exposure geometric moiré [1] can produce valuable and meaningful patterns of fringes. It is a well-established technique with various applications [2]. There exist numerous technical solutions for dynamic moiré analysis [3]. A typical example is when a free surface of liquid is illuminated through a grid focusing an array of light and dark lines on the surface. Interpretation of the dynamic picture (or series of static pictures) of grating can bring lots of useful information about the motion of the surface. Another widely used application is the analysis of transient mechanics of deformation exploiting laser moiré interferometry [4–6].

Nevertheless, direct dynamic interpretation of structural vibrations from dynamic pictures of moiré grating is hardly possible due to a relatively high frequency of resonance oscillations of the analysed structures. An alternative could be the coupling of time-average techniques and geometric moiré fringe analysis. It can be noted that direct geometric moiré analysis (not laser moiré interferometry) is considered when a grating of dark and white lines is plotted onto the surface of the analysed body. Yet there are a few open questions. Will the patterns of fringes be formed as the time-average techniques are used? And if the pattern of fringes is formed, how can it be interpreted ? This paper tries to answer these questions and to prove the applicability of time-average geometric moiré for analysis of vibrating elastic structures. Such a method of measurement does not require complex experimental set-up and can provide valuable results in many practical applications.

## 2. One-dimensional model

For simplicity, a one-dimensional system is analysed first. The moiré grating in the state of equilibrium is defined as a harmonic variation of grey scale in the range between 0 (representing black colour) and 1 (representing white colour). Such a definition of grating is well suited for numerical reconstruction of moiré fringes [7]. The intensity is a continuous function, and line width is 50% of the pitch.

Superposition of two gratings (double exposure of the gratings in the state of equilibrium and in the deformed state) produces a moiré fringe pattern:

$$\begin{aligned} I_s(x,u) &= \frac{1}{2}\left(\cos^2\left(\frac{\pi}{\lambda}\,x\right)+\cos^2\left(\frac{\pi}{\lambda}(x-u)\right)\right) \\ &= \frac{1}{2}+\frac{1}{2}\cos\left(\frac{2\pi}{\lambda}\left(1-\frac{u}{2x}\right)x\right)\cos\left(\frac{\pi}{\lambda}\,u\right), \end{aligned} \tag{1}$$

where $I_s$ is the intensity in double exposure geometric moiré, $x$, the longitudinal co-ordinate, $u$, the displacement from the state of equilibrium at point $x$ and $\lambda$ is the parameter defining the pitch of grating. The first term in Eq. (1) represents the grey-scale level of the surface in the state of equilibrium and the second term represents that in the state of deformation. Such a formulation of intensity enables straightforward embedding of the results from finite element analysis to digital computer plotting procedures. The centres of fringes will coincide with the locations

where the intensity will be equal to 0.5. Thus, the relationship among fringe orders, the pitch of the grating and the displacement can be derived from the condition $\cos((\pi/\lambda)u) = 0$:

$$u = \lambda\left(n - \frac{1}{2}\right); \quad n = 1, 2, \ldots, \tag{2}$$

where $n$ is the fringe order. Each new fringe indicates an increase or decrease of specimen displacement by one grating pitch (component of the displacement perpendicular to the reference grating lines). If the displacement from the state of equilibrium $u$ is assumed to be a linear function of $x$, the resulting intensity distribution takes the form of beatings (Fig. 1). Such an effect can be successfully exploited in the procedures building computer-generated moiré fringes from finite element calculations [7].

Alternatively, double-exposure geometric moiré can be constructed as a superposition of two gratings, one of which is in the deformed state and the other is also in the deformed state but with the opposite deformation. Then the following fringe pattern will be produced:

$$\begin{aligned} I_{so}(x,u) &= \frac{1}{2}\left(\cos^2\left(\frac{\pi}{\lambda}(x-u)\right) + \cos^2\left(\frac{\pi}{\lambda}(x+u)\right)\right) \\ &= \frac{1}{2} + \frac{1}{2}\cos\left(\frac{2\pi}{\lambda}\,x\right)\cos\left(\frac{2\pi}{\lambda}\,u\right) \end{aligned} \tag{3}$$

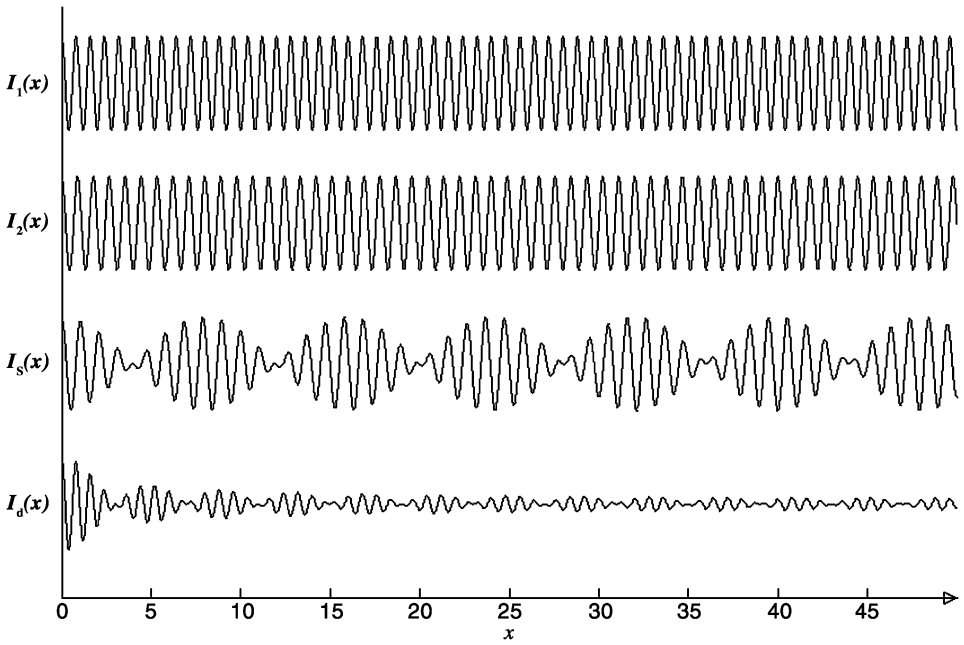


Fig. 1. $I_1(x)$, $I_2(x)$, $I_S(x)$ and $I_d(x)$ at $\lambda = 0.8$ and $u = kx$ at $k = 0.1$.

where $I_{so}$ is the intensity of double exposure moiré when gratings with opposite deformations are superposed. Thus, the relationship among fringe orders, the pitch of the grating and the displacement takes the following form:

$$u = \frac{\lambda}{2}\left(n - \frac{1}{2}\right); \quad n = 1, 2, \ldots. \tag{4}$$

Let us consider the previously mentioned one-dimensional model with the assumption that an elastic structure performs harmonic oscillations and the amplitudes (maximum displacements from the status of equilibrium) are $u(x)$. If the time of exposition is much longer than the period of oscillations, the resulting pattern is formed as an integral sum of the continuous process of motion:

$$\begin{aligned} I_d(x,u) &= \lim_{T\to\infty}\frac{1}{2T}\int_0^T \left(1+\cos\left(\frac{2\pi}{\lambda}(x-u\sin(\omega t+\varphi))\right)\right)\mathrm{d}t \\ &= \frac{\omega}{2\pi}\int_{-\varphi/\omega}^{(2\pi-\varphi)/\omega} \cos^2\left(\frac{\pi}{\lambda}(x-u\sin(\omega t+\varphi))\right)\mathrm{d}t \\ &\approx \frac{\omega}{2\pi}\sum_{i=1}^{m}\left\{\cos^2\left(\frac{\pi}{\lambda}x - u\sin\left(\omega\left(-\frac{\varphi}{\omega}+(i-1)\frac{2\pi}{m\omega}\right)+\varphi\right)\right)\frac{2\pi}{m\omega}\right\} \\ &= \frac{1}{m}\sum_{i=1}^{m}\left\{\cos^2\left(\frac{\pi}{\lambda}\left(x-u\sin\left(\frac{2\pi}{m}(i-1)\right)\right)\right)\right\}, \end{aligned} \tag{5}$$

where $I_d$ is the intensity of illumination in dynamic moiré fringe analysis, $T$, the exposure time, $\omega$, the angular frequency of oscillations, $\varphi$, the phase and $m$, the number of discrete states in a period of oscillations.

The first equality in Eq. (5) follows from the periodicity of harmonic function. The second approximate equality builds the ground for approximate numerical technique of the reconstruction of the pattern of fringes. The greater the value of $m$, the better the quality. It can be noted that neither $\omega$ nor $\varphi$ has any effect on the pattern of fringes. But

$$\begin{aligned} &\lim_{T\to\infty}\frac{1}{2T}\int_0^T \left(1+\cos\left(\frac{2\pi}{\lambda}(x-u\sin(\omega t+\varphi))\right)\right)\mathrm{d}t \\ &\quad= \frac{1}{2} + \lim_{T\to\infty}\frac{1}{2T}\int_0^T \cos\left(\frac{2\pi}{\lambda}\,x\right)\cos\left(\frac{2\pi}{\lambda}(u\sin(\omega t+\varphi))\right)\mathrm{d}t \\ &\qquad+ \lim_{T\to\infty}\frac{1}{2T}\int_0^T \sin\left(\frac{2\pi}{\lambda}\,x\right)\sin\left(\frac{2\pi}{\lambda}(u\sin(\omega t+\varphi))\right)\mathrm{d}t \\ &\quad= \frac{1}{2} + \frac{1}{2}\cos\left(\frac{2\pi}{\lambda}\,x\right)J_0\left(\frac{2\pi}{\lambda}\,u\right), \end{aligned} \tag{6}$$

where $J_0$, is the zero-order Bessel function of the first kind:

$$J_0(a) = \lim_{T\to\infty}\left(\frac{1}{T}\int_0^T \exp(\mathrm{j}a\sin(\omega t+\varphi))\mathrm{d}t\right) \tag{7}$$

It can be noted that integrals

$$\lim_{T\to\infty}\frac{1}{2T}\int_0^T \sin\left(\frac{2\pi}{\lambda}\,(u\sin(\omega t+\varphi))\right)\mathrm{d}t \quad \text{and}$$
$$\lim_{T\to\infty}\frac{1}{T}\int_0^T \sin(a\sin(\omega t+\varphi))\,\mathrm{d}t$$

converge to zero due to the non-evenness of the sine function.

The surface intensities for double exposure and time-average geometric moiré are illustrated in Fig. 1, where $I_1(x)$ is the equilibrium state and $I_2(x)$ the deformed state.

Eq. (6) enables explicit construction of the envelope function which modulates the grating $\cos((2\pi/\lambda)x)$ and characterises the formation of fringes:

$$E(u)=\frac{1}{2}\pm\frac{1}{2}J_0\left(\frac{2\pi}{\lambda}\,u\right) \tag{8}$$

where $E$ stands for the envelope function (Fig. 2a). Though the decay of intensity of illumination at increasing amplitudes is quite strong, it is not as fast as in time average holography[1], where the decay of intensity of illumination is defined as

$$H(u)=\left(J_0\left(\frac{2\pi}{\lambda}\,u\right)\right)^2, \tag{9}$$

where $H$ is the intensity of illumination in the time-average holographic image. It is important to note that the intensity of illumination in time-average moiré applications converges to 0.5 (instead of 0 in holographic analysis) at increasing amplitudes, and special digital image brightening techniques [8] can be avoided.

From Eq. (6), it is clear that the accuracy of numerical reconstruction of the image is determined by the parameter $m$—the number of discrete states in a period of oscillations ascertains the character of the reconstructed envelope function (explicitly defined by Eq. (8)). The procedure of numerical reconstruction presented in Eq. (6) does not explicitly define the envelope function. But it is still possible to define that function using a similar technique as used in Eq. (8). It can be noted that the extreme values of the last term in Eq. (6) occur at $x=0$ and $x=\lambda/2$. Then,

$$E_m(u)=\begin{cases}\frac{1}{m}\sum_{i=1}^{m}\left(\cos^2\left(\frac{\pi}{\lambda}\,\sin\left(\frac{2\pi}{m}(i-1)\right)u\right)\right)\\ \frac{1}{m}\sum_{i=1}^{m}\left(\sin^2\left(\frac{\pi}{\lambda}\,\sin\left(\frac{2\pi}{m}(i-1)\right)u\right)\right)\end{cases} \tag{10}$$

where $E_m$ is the reconstructed envelope function at predefined $m$. Fig. 2a presents the numerically reconstructed envelope lines at $m=22$, which guarantees sufficient accuracy of reconstruction of the first five fringes. The relationship between the number of correctly reconstructed fringes and the number of discrete states in a period of harmonic oscillations is presented in Fig. 2b.

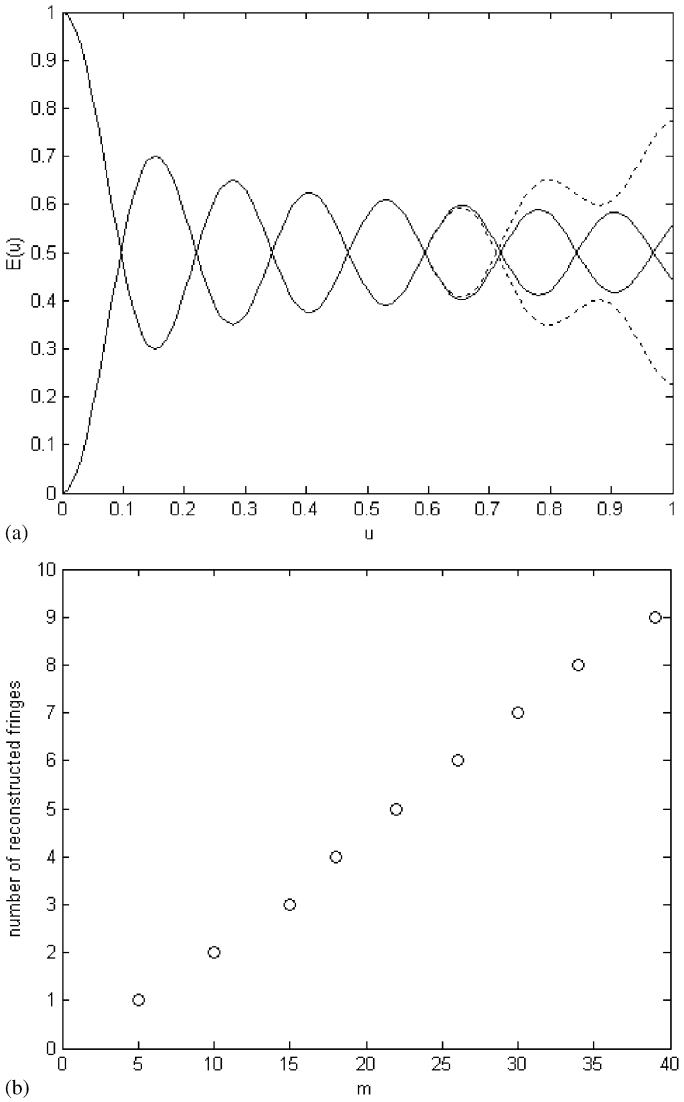


Fig. 2. (a) Envelope function at $\lambda = 0.25$; solid line stands for the analytical definition and dashed lines for the numerical reconstruction at $m = 22$. (b) Relationship between the number of correctly reconstructed fringes and parameter $m$.

## 3. Interpretation of the fringe pattern (quantitative analysis of deformation)

The fringe pattern produced by time-average geometric moiré is directly related to the displacement field, as in double exposure geometric moiré. The only difference is that the relationship between the number of fringes and the value of displacement in

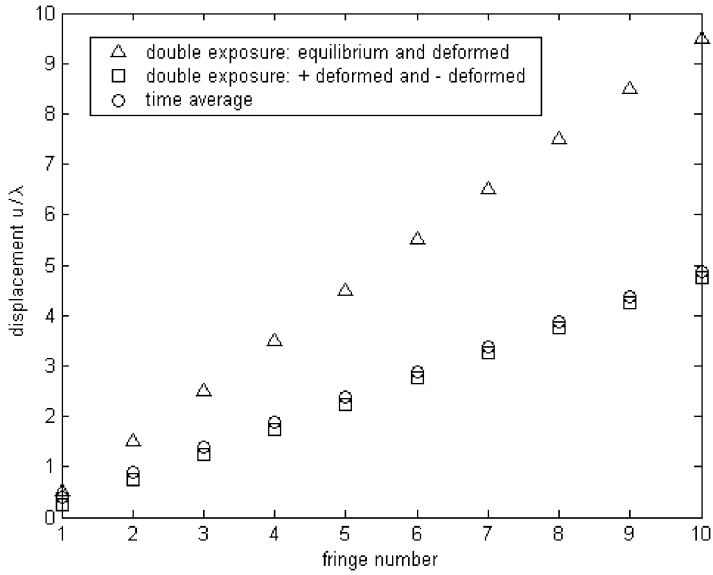


Fig. 3. Relationship between the non-dimensional displacement and the fringe number.

time-average moiré analysis is non-linear. Explicitly, this relationship can be derived from Eq. (8). The centres of the fringes coincide with the isolines corresponding to the solution of equality $E(u) = \frac{1}{2}$. Thus, the explicit relationship among the fringe order, pitch of the grating and dynamic displacement is obtained from the condition requiring that the value of the Bessel function is zero:

$$u = \frac{\lambda}{2\pi} r_n, \tag{11}$$

where $r_n$ is the $n$th root of the zero-order Bessel function of the first kind. It can be noted that the values of the roots of the zero-order Bessel function of the first kind are available in classical texts [9]. The relationship between the non-dimensional dynamic displacement and the fringe number is presented in Fig. 3.

It can be noted that the object of moiré analysis is to measure displacement components normal to the grating lines. Both components of the two-dimensional displacement vector can be determined from two experiments with mutually orthogonal gratings. This is true both for double exposure and time-average geometric moiré.

## 4. Experimental validation of the method

The goal of experimental time-average moiré analysis is to validate the method. A grating of dark and white lines is drawn on the surface of rubber specimens which are mounted to a shaker system (Fig. 4).

Fig. 4. View of the experimental set-up.

One rubber specimen is produced with horizontal grating and another with vertical grating. The grating pitch is 1 mm, line width is half of the pitch, and driving frequency of the shaker table is 51 Hz, which corresponds to the second resonance frequency of the rubber specimens. A digital photo camera with exposition time $T = 1.5$ seconds is used. The produced images are presented in Figs. 5a and b. It can be noted that the high sharpness of the grating is preserved in the motionless zones of the rubber specimen. The fringes can be identified with the naked eye in live experiments, although for higher fringe numbers their contrast decreases.

The produced experimental time-average moiré fringes enable the straightforward interpretation of dynamic deformations. For example, nine fringes are visible to the left of the motionless zone in Fig. 5a. This means that the maximum dynamic displacement of the end of the rubber specimen in the vertical direction is $u/\lambda = r_9/2\pi$ (from Eq. (11)), and here $r_9 \approx 27,4927$. Thus, the maximum dynamic displacement from the status of equilibrium is 4,3756 pitches, or 8,7512 pitches from maximum displacement "up" and maximum displacement "down" in the vertical direction. It is easy to count the grating lines between the maximum deflections at the region of the end section of the rubber specimen. The number of lines is about 8. That shows perfect coincidence between experimental and theoretical results.

## 5. Experimental analysis of lithographic press rubber roller

Circular time-average moiré has many advantageous features over other experimental methods for the analysis of rotating circular objects. This is clearly illustrated in a time-average photo of a rotating lithographic press rubber roller train (Fig. 6). No interpretable patterns would be formed at all if the moiré grating were not formed as an array of concentric circles.

The intensity of illumination for time-average circular geometric moiré with concentric grating can be expressed as an integral average of variation of radial

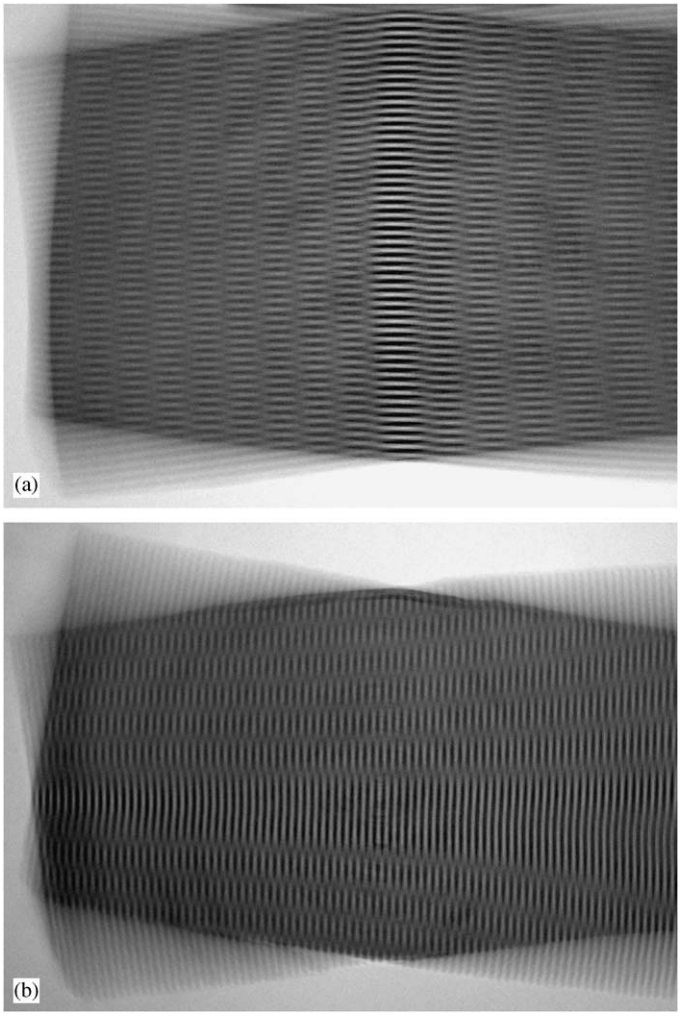


Fig. 5. (a)Experimental time-average moiré fringes (vertical grating). (b) Experimental time-average moiré fringes (horizontal grating).

displacements:

$$I_{\mathrm{dr}}(x,y,u,v) = \lim_{T\to\infty}\frac{1}{2T}\int_0^T\left(1+\cos\left(\frac{2\pi}{\lambda}\sqrt{(x-u(t))^2+(y-v(t))^2}\right)\right)\mathrm{d}t, \tag{12}$$

where $I_{\mathrm{dr}}$ is the intensity of illumination for time-average circular geometric moiré with concentric grating, $\lambda$ is a constant determining the distance between concentric lines in the status of equilibrium, and $u(t)$ and $v(t)$ are in-plane dynamic

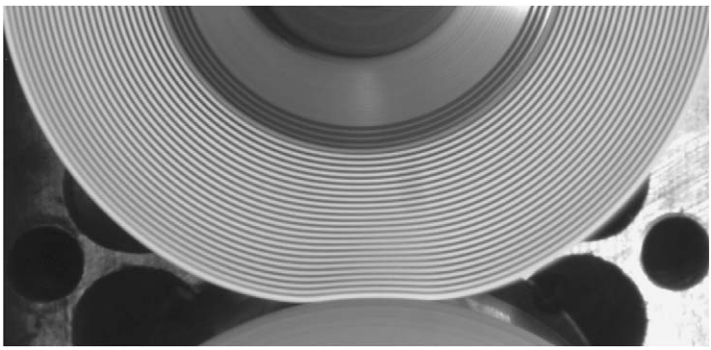

Fig. 6. Time-average photo of a rotating lithographic press rubber roller train.

Fig. 7. Time-average photograph of the vibrating rubber roller.

displacements in cartesian frame. It can be noted that concentric grating enables the registration of radial displacements and is insensitive to angular displacements (rotation). Alternatively, radial moiré grating can be used for circular objects. Such grating would be sensitive to angular, not radial displacements (but not applicable for rotating objects):

$$I_{\mathrm{da}}(x,y,u,v) = \lim_{T\to\infty}\frac{1}{2T}\int_0^T \left(1+\cos\left(k\tan^{-1}\frac{x-u(t)}{y-v(t)}\right)\right)\mathrm{d}t, \tag{13}$$

where $I_{\mathrm{da}}$ is the intensity of illumination for time-average circular geometric moiré with radial grating and $k$ is a constant determining the number of radial lines.

If the roller train vibrates, time-average circular geometric moiré with concentric grating can provide valuable information about dynamic deformations. This is

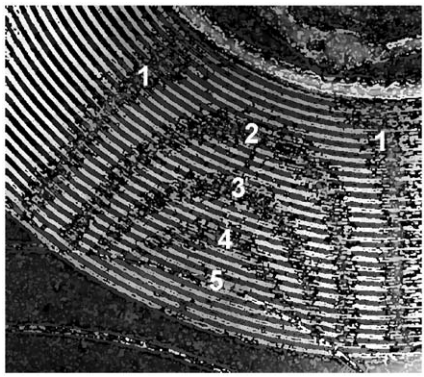


Fig. 8. Digitally processed image of the contact zone with enumerated fringes.

illustrated in Fig. 7, where the rubber roller does not turn and its axis is motionlessly fixed. The pitch of circular grating is 1 mm, and line width is half the pitch. The steel roller performs harmonic vibrations, the frequency of vibrations is 20 Hz, and exposure time is 2 s. Interference fringes in the contact zone are clearly visible with the naked eye. Noteworthy is the image of the steel roller where two maximum deflections from the status of equilibrium are best registered in the time-average photo due to the fact that the velocity of the vibrating body is small around the regions of maximum displacements.

Digital processing of the image of the contact zone (Fig. 8) provides an even clearer picture of the interference fringes. It can be noted that the interpretation of fringes is different from double-exposure geometric moiré as the formation of fringes is governed by time-average moiré and is defined explicitly by Eq. (11). For concentric grating every fringe will determine dynamic displacement in the radial direction and the magnitude of displacement can be found from Eq. (11). Ordinary fringe counting techniques can be used for determination of the fringe order.

It is important to note that time-average geometric moiré is a non-contact whole-field technique and provides information on dynamic deformations which can be easily registered and quantified in the domain of the whole analysed object. The advantages of this optical technique are especially clear when applied for the analysis of dynamic deformations of the rubber layer of the lithographic press roller.

## 6. Concluding remarks

Time-average geometric moiré for analysis of in-plane vibrations of elastic structures is proposed in this paper. Apparently, the fact that the intensity of higher fringes is blurred was hiding this method amongst other non-contact whole-field experimental techniques for analysis of structural vibrations.

This paper proves that such a method is feasible for the analysis of vibrations. It has many advantageous features — it is a straightforward method and does not

require a complex experimental set-up. It is even more simple than double-exposure geometric moiré—no artificial superposition of the reference image and the image of the object in the deformed state is necessary. Naturally, the interpretation of fringe patterns in time-average geometric moiré is different from the double-exposure geometric moiré. But this fact does not decrease the practical value of the method, which can be effectively exploited for the analysis of vibrating elastic structures.

## References

[1] Kobayashi AS, editor. Handbook on experimental mechanics. 2nd ed. SEM; 1993.
[2] Post D, Han B, Ifju P. High sensitivity moiré: experimental analysis for mechanics and materials. Berlin: Springer Verlag; 1997.
[3] Indebetoun G, Czarnek R. Selected papers on optical moiré and applications. Virginia Polytechnic Institute and State University; 1992.
[4] Huimin X, Guotao W, Fulong D, Guangjun Z, Xingfu L, Fangju Z, et al. The dynamic deformation measurement of the high speed heated LY12 aluminium plate with moiré interferometry. J Mater Process Technol 1998;83(1–3):159–63.
[5] Deason VA, Epstein JS, Abdallah A. Dynamic diffraction moiré: theory and applications. Opt Lasers Eng 1990;12(2–3):173–87.
[6] Kokaly MT, Lee J, Kobayashi AS. Moiré interferometry for dynamic fracture study. Opt Lasers Eng 2003;40(4):231–47.
[7] Ragulskis M, Maskeliunas R, Ragulskis L. Plotting moiré fringes for circular structures from FEM results. Exp Techniques 2002;26(1):31–5.
[8] Ragulskis M, Palevicius A, Ragulskis L. Plotting holographic interferograms for visualization of dynamic results from finite-element calculations. Int J Numer Meth Engng 2003;56:1647–59.
[9] West CM. Holographic interferometry. New York: Wiley; 1979.